

Charge transfer rate modulated energy loss in indoor organic photovoltaic cells

Cite as: Appl. Phys. Lett. **127**, 083902 (2025); doi: [10.1063/5.0282998](https://doi.org/10.1063/5.0282998)

Submitted: 29 May 2025 · Accepted: 11 August 2025 ·

Published Online: 25 August 2025






View Online



Export Citation



CrossMark

Kangning Zhang,¹ Jiawei Qiao,¹ Sixuan Cheng,² Mingxu Zhou,¹ Jinqun Xu,¹ Peng Lu,³  Hang Yin,¹  Xiaoyan Du,¹  Maojie Zhang,² and Xiaotao Hao^{1,4,a)} 

AFFILIATIONS

¹School of Physics, State Key Laboratory of Crystal Materials, Shandong University, Jinan, Shandong 250100, China

²National Engineering Research Center for Colloidal Materials, Key Laboratory of Special Functional Aggregated Materials (Shandong University), Ministry of Education, School of Chemistry & Chemical Engineering, Shandong University, Jinan, Shandong 250100, China

³School of Physics, National Demonstration Center for Experimental Physics Education, Shandong University, Jinan, Shandong 250100, China

⁴School of Chemistry, The University of Melbourne, Parkville, Victoria 3010, Australia

Note: This paper is part of the Special Topic, High-Performance Thin-Film Indoor Photovoltaics.

a) Author to whom correspondence should be addressed: haotxt@sdu.edu.cn

ABSTRACT

Minimizing energy loss is pivotal for achieving high-performance indoor organic photovoltaic (IOPV) cells, where charge transfer (CT) rate critically governs exciton-to-charge conversion efficiency. Nevertheless, the fundamental correlation between CT rate and energy loss remains insufficiently understood. In this study, we systematically investigate how CT rate affects the radiative and non-radiative energy loss in IOPV devices employing PBDB-T donor and three wide-bandgap BTA3 series acceptors. A developed global fitting model for charge separation pathways demonstrates that the intra-moiety delocalized excitations and CT states show comparable contributions to exciton dissociation efficiency (each accounting for approximately 50%). Notably, our findings reveal that excessive driving forces can paradoxically reduce CT rate, resulting in prolonged existence of CT states at the donor:acceptor interfaces that amplifies radiative and non-radiative recombination. The lower CT rate-mediated energy loss becomes increasingly dominant under indoor weak illumination compared to standard solar conditions due to reduced density of CT states and intensified influence of trap states. This elucidates a CT rate-dependent energy loss mechanism that warrants greater consideration in the design of IOPVs. These results highlight the importance of CT rate modulation for suppressing energy loss, providing valuable insights for the rational design of photovoltaic materials for diverse indoor energy harvesting applications.

Published under an exclusive license by AIP Publishing. <https://doi.org/10.1063/5.0282998>

The rise of the Internet of Thing (IoT) presents an enormous demand for off-grid energy sources to drive various indoor electronic devices with low-power (1–100 μ W) consumption. Under multiple indoor scenarios, organic photovoltaic (OPV) cells have already demonstrated remarkable efficacy as light-harvesting devices when exposed to illumination from light-emitting diodes (LEDs) and fluorescent lamps,^{1–5} due to their tunable optical bandgaps, strong light absorption characteristics, diverse color options, and superior mechanical flexibility.^{6–8} Their inherent advantages guarantee that OPV cells deliver adequate energy output to sustainably power the IoT electronic devices while exhibiting optimal compatibility with various indoor application scenarios. Despite achieving power conversion efficiencies (PCEs) surpassing 30% at the present stage,^{9,10} the performance of indoor organic

photovoltaic (IOPV) devices remains suboptimal with respect to the theoretical efficiency limits of exceeding 40%.^{11,12} To further improve photovoltaic performance of IOPV cells, some feasible approaches have been employed to modulate the following characteristics. First, efficient wide-bandgap donors and non-fullerene acceptors (NFAs) were designed and synthesized to match the illumination spectrum (400–750 nm) of indoor light sources, yielding high and matching external quantum efficiency (EQE) spectrum.¹³ Second, ternary strategy was applied to optimize energetic offsets and molecular packing to suppress trap-mediated recombination in low carrier densities.¹⁴ Third, considering that the reduced light intensity normally induces an additional energy loss of approximately 0.16 V under indoor light illumination,¹⁵ it is essential and desirable to minimize energy loss during

exciton-to-charge conversion process to acquire a maximum open-circuit voltage (V_{OC}). While comprehensive investigations have been conducted on energy loss mechanisms and their mitigation strategies in state-of-the-art outdoor OPV devices,^{16,17} the understanding of energy loss remains unclear in IOPV cells. This knowledge gap mainly originates from the fundamental differences in device design rules between outdoor and indoor OPV technologies, necessitating an in-depth investigation for indoor energy harvesting applications.

From the perspective of exciton dynamics analysis, the understanding of energy loss in IOPVs is more complex compared to outdoor OPVs, as it is challenging to selectively excite acceptors to discriminate between electron and hole transfer process. When designing the well-matched active layer materials to maximize the V_{OC} in IOPVs, two fundamental characteristics should be considered emphatically including wide bandgaps and appropriate molecular energy levels. Generally, the energetic offsets of the lowest unoccupied molecular orbital (LUMO) or highest occupied molecular orbital (HOMO) provide the driving force for exciton dissociation. The underlying relationship between the charge transfer (CT) rate (k_{CT}) and the driving force (ΔG) can be quantitatively described by the classical Marcus electron-transfer theory,^{18–20}

$$k_{CT} = V^2 \sqrt{\frac{\pi}{\lambda k_B T}} \exp \left[-\frac{(\Delta G + \lambda)^2}{4\lambda k_B T} \right],$$

where ΔG is the driving force, λ is the reorganization energy, V represents the electronic coupling between the initial and final states. According to this theory, k_{CT} exhibits a progressive increase when ΔG exceeds $-\lambda$, reaches its peak magnitude at $\Delta G \approx -\lambda$, and undergoes a gradual attenuation as ΔG falls below $-\lambda$. Notably, a strategic reduction of the driving force for exciton dissociation via electron and hole transfer, while maintaining a high CT rate, enables effective mitigation of energy loss.^{21,22} Currently, there is still no direct observation that can rationalize the underlying correlation between CT rate and energy loss in IOPVs due to the intertwined contributions of two competitive exciton dissociation pathways involving CT states and intra-moiety delocalized excitations (i-DEs) separating into charge carriers. Hence, a photophysical correlation picture between them is thus required to aid the further improvement of IOPV device efficiencies.

In this work, we investigate the influence of CT rate on energy loss in IOPV cells based on the PBDB-T donor in blending with the wide-bandgap BTA3, F-BTA3, and Cl-BTA3 acceptors. Regarding the complex spectral and kinetic information from transient absorption spectroscopy (TAS), a global fitting model has been developed and reveals that the i-DE- and CT-mediated channels contribute equally to exciton dissociation efficiency (each constituting approximately 50%). Combined with the analysis of TAS data and time-resolved photoluminescence (TRPL) spectra, we observe that the gradually enlarged energetic offsets of LUMO or HOMO between donor and acceptor decrease CT rate and prolong the duration of CT states at the donor:acceptor (D:A) interfaces, leading to enhanced radiative and non-radiative recombination. Research on energy loss at the device level demonstrates that recombination processes caused by limited CT rate play an obvious role in reducing the V_{OC} of IOPV cells compared to outdoor OPV devices, primarily attributed to diminished exciton density and dominated trap-induced recombination under low-intensity illumination conditions. Moreover, it is also found that increasing

energetic disorder of the first excited state (S_1) does not proportionally elevate the recombination loss of CT state in IOPV systems. This means that the design of IOPV cells alleviates the constraints on the Stokes shift of donor and acceptor materials. These findings present a rational understanding of CT rate-dependent energy loss process and potentially help to improve the performance of IOPV cells.

Figures 1(a) and S1 present the chemical structures and the electrostatic potential of the donor PBDB-T and three series acceptors comprising BTA3, F-BTA3, and Cl-BTA3 used in this work, respectively. Halogenation engineering, as a strategic molecular modification approach, has demonstrated significant efficacy in modulating the electronic energy levels and the photon-harvesting capabilities of photovoltaic molecules.²³ As shown in Fig. 1(b), fluorination and chlorination progressively lower the LUMO and HOMO energy levels of BTA3 derivatives. This systematic energy-level depression induces monotonic increase in both the LUMO and HOMO energetic offsets ($\Delta LUMO$ and $\Delta HOMO$) across the corresponding D:A blend systems, evolving from PBDB-T:BTA3 to PBDB-T:F-BTA3 and then to PBDB-T:Cl-BTA3 (Table S1). The absorption spectra of neat and blend films are primarily concentrated within the wavelength range of 450–700 nm [Figs. 1(c) and 1(d)], demonstrating a close alignment with the emission spectra of common indoor illumination sources. Although the overlapping optical absorption features in IOPVs complicate the differentiation of electron and hole transfer process, the concurrent elevation of both the $\Delta LUMO$ (0.28–0.45 eV) and $\Delta HOMO$ (0.19–0.34 eV) permits quantitative deconvolution of overall CT dynamics through systematic spectroscopic analysis in these three systems.

Femtosecond transient absorption spectroscopy was employed to investigate the dynamics of excitons and photocarriers in three OPV systems. As illustrated in Fig. 2(a), we developed a global fitting model to deconvolute two competing exciton dissociation pathways: (1) local excitons (LEs) undergoing sequential transformation via i-DEs prior to charge-separated (CS) states ($LE \rightarrow i-DE \rightarrow CS$) and (2) direct LE-to-CT state conversion followed by the interfacial dissociation ($LE \rightarrow CT \rightarrow CS$). Because the temporal scale of the conversion process from LE to i-DE is within 0.2 ps,²⁴ our global kinetic model assigns 0.2 ps as the time reference for system initialization, providing sufficient resolution to decouple the two charge separation pathways. Figures S2 and 2(b) exhibit two-dimensional (2D) color plots of raw and globally fitted TAS data in PBDB-T:BTA3 system. Critical validation emerges from the quantitative agreement between the experimental spectral features at selective delay times [Fig. 2(c)] and kinetic profiles at characteristic wavelengths [Fig. 2(d)] with their simulated counterparts, which confirm the reliability of our model. Through this analytical model, we further resolve the spectro-temporal characteristics of four distinct excited-state species (LE, i-DE, CT, and CS) as shown in Figs. 2(e) and 2(f). This analytical approach has been consistently applied to the PBDB-T:F-BTA3 and PBDB-T:Cl-BTA3 systems, with complete datasets and fitting results presented in Figs. S3 and S4. Therefore, building upon the above validated global kinetic framework, we can achieve quantitative research on exciton and charge dynamics in IOPVs.

The relative contributions of two exciton dissociation pathways across all three investigated systems are quantitatively summarized in Fig. 3(a) and Table S2. Statistical analysis reveals near-equivalent population distribution between two dissociation channels: Channel 1 ($LE \rightarrow i-DE \rightarrow CS$) and Channel 2 ($LE \rightarrow CT \rightarrow CS$), each contributing

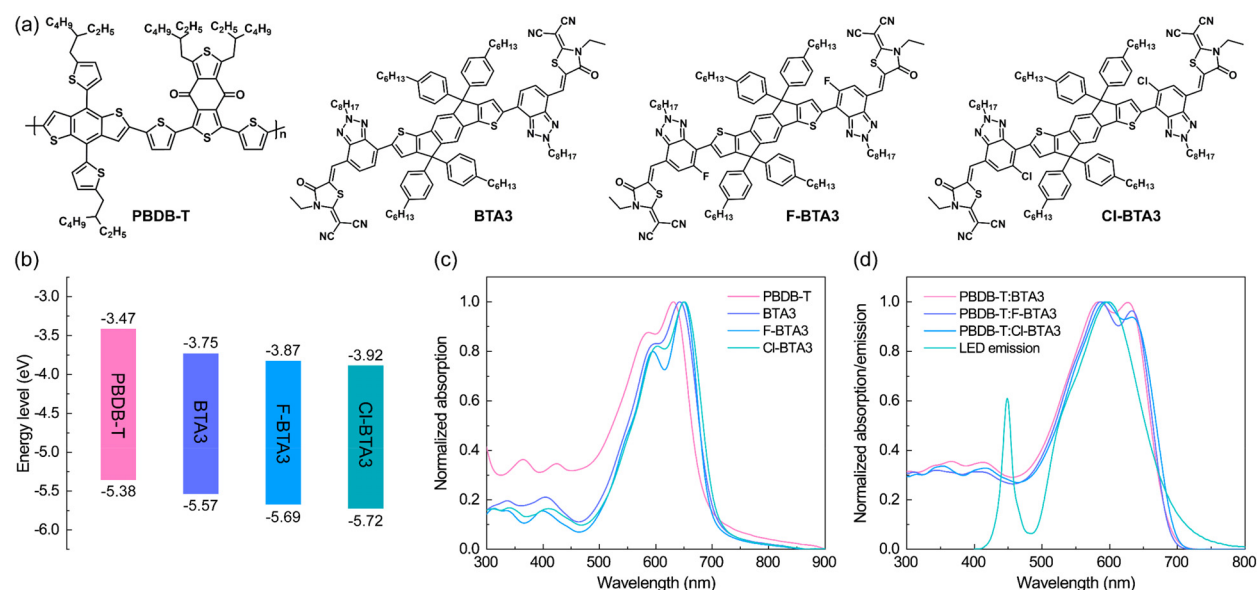


FIG. 1. (a) Chemical structures and (b) energy levels of PBDB-T, BTA3, F-BTA3, and Cl-BTA3 used in this work. (c) Normalized absorption spectra of neat films. (d) Normalized emission spectra of LED source and absorption spectra of blend films.

about 50% to the total exciton dissociation yield. Figure 3(b) exhibits the characteristic lifetimes of four different excited-state species: τ_1 (0.48–0.58 ps) for LE, τ_2 (5.79–8.46 ps) for i-DE, τ_3 (190.61–386.65 ps) for CT, and τ_4 (9290.23–9926.54 ps) for CS states. The kinetic traces of

the ground state bleaching (GSB) signals probed at 630 nm, which reflect total photocarrier population dynamics encompassing two exciton dissociation pathways, are compared in Fig. 3(c). Notably, both raw GSB kinetic traces and globally fitted lifetimes manifest that the

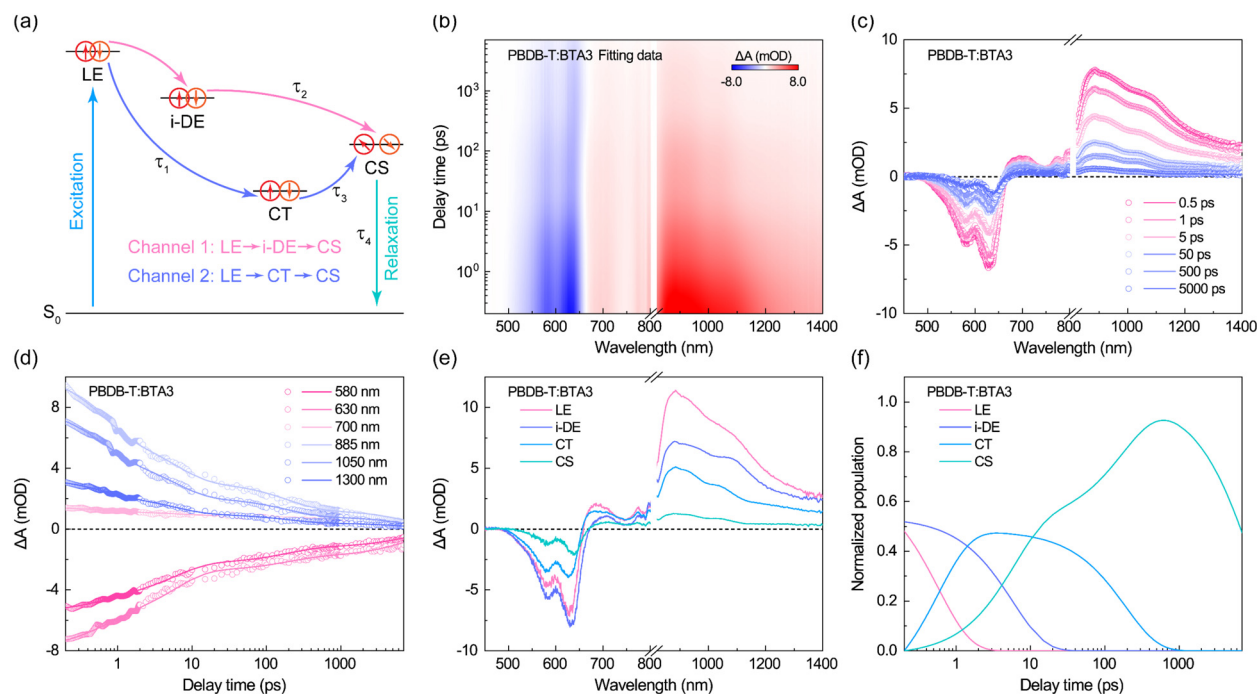


FIG. 2. (a) Global fitting model for exciton dissociation. (b) Globally fitting 2D color plots for PBDB-T:BTA3. (c) TA spectra at selective delay times, (d) TA dynamics at selective detection wavelengths before (dot) and after (line) global fitting. (e) Spectral and (f) temporal features of LE, i-DE, CT, and CS states.

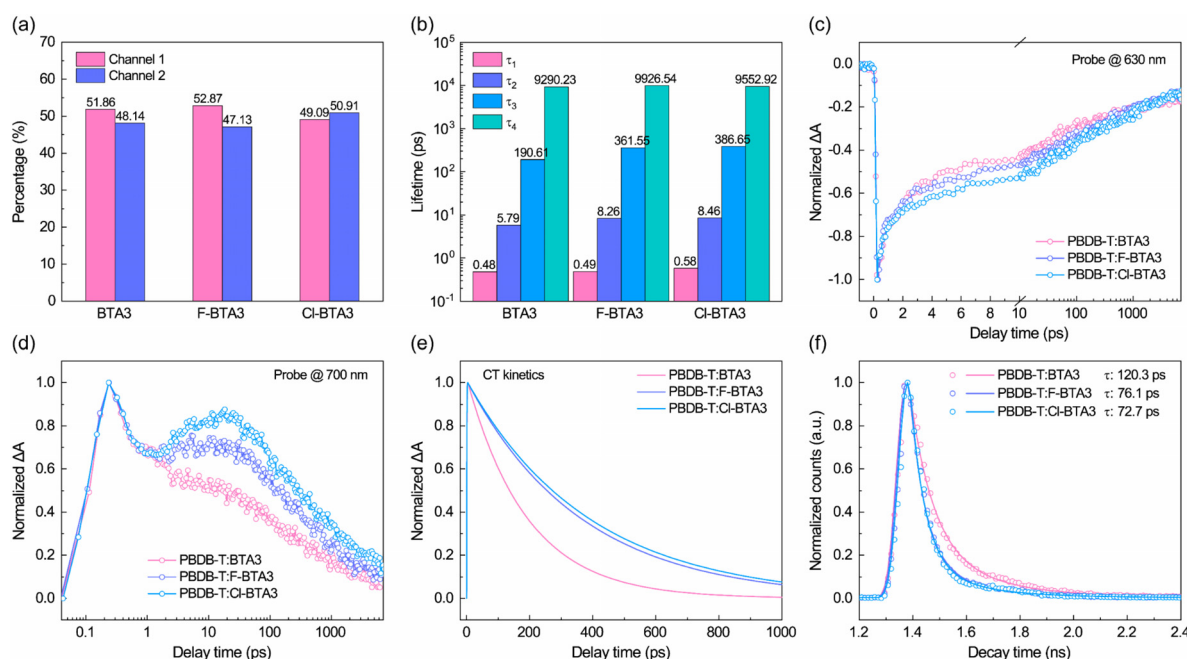


FIG. 3. (a) Global fitting proportion of two exciton dissociation channels. (b) Global fitting lifetime of LE, i-DE, CT, and CS states. TA dynamics probed at (c) 630 nm and (d) 700 nm. (e) Global fitting CT kinetics. (f) TRPL spectra for three OPV systems.

energetic offset variations predominantly modulate the CT rate. To directly monitor the temporal evolution of CT states, we analyze and compare the raw excited state absorption (ESA) signals at 700 nm, a spectral region where CT states dominate the photophysical response [Figs. 2(e), S3e, and S4e]. Figure 3(d) demonstrates that the PBDB-T:F-BTA3 and PBDB-T:Cl-BTA3 blends present distinct resaturation dynamics in their kinetic traces, occurring on a timescale of tens of picoseconds after photoexcitation. This kinetic feature stems predominantly from the accumulation of CT states at the D:A interfaces, a direct consequence of the markedly reduced CT rates quantified in Fig. 3(e). Complementary to TAS analysis, we also conducted TRPL spectra measurements to investigate CT dynamics through fluorescence decay characteristics. The TRPL spectra reveal a progressive reduction in fluorescence lifetime from 120.3 ps for PBDB-T:BTA3 to 76.1 ps for PBDB-T:F-BTA3 and then to 72.7 ps for PBDB-T:Cl-BTA3 probed at the maximum PL peaks [Fig. 3(f), Table S3]. Meanwhile, consistent spectral characteristics are observed in the fluorescence lifetime probed at 690 nm (Fig. S5, Table S3). This monotonic decrease in fluorescence lifetime exhibits an inverse correlation with the finding of CT rate derived from TAS data, indicating the increased radiative and non-radiative recombination of CT states under large energetic offsets or driving forces.²⁵

To investigate the photovoltaic performance under one sun and indoor light illumination, we fabricated proof-of-concept OPV cells with a conventional structure of ITO/PEDOT:PSS/active layer/PDINN/Ag. The detailed fabrication process is shown in the supplementary material. Figure 4(a) exhibits the current density vs voltage (J - V) curves of OPV cells under AM 1.5 G 100 mW cm⁻² illumination, and the corresponding device parameters are provided in Table S4. The optimal PBDB-T:BTA3 cells achieve a PCE of 9.32%,

with a V_{OC} of 1.132 V, a short-circuit current density (J_{SC}) of 13.12 mA cm⁻², a fill factor (FF) of 62.72%. Compared to PBDB-T:BTA3, the V_{OC} reduces to 1.044 V for PBDB-T:F-BTA3 and 1.008 V for PBDB-T:Cl-BTA3, which is attributed to the gradually decreasing energetic offsets between the HOMO of donor and the LUMO of acceptor. In contrast, PBDB-T:F-BTA3 and PBDB-T:Cl-BTA3 present the enlarged J_{SC} of 13.73 and 13.95 mA cm⁻², as well as FF of 65.56% and 64.79%. These benefits mainly arise from the improved optical response evidenced by the external quantum efficiency (EQE) spectra [Fig. 4(b)] and optimized charge transport confirmed by carrier mobility results (Fig. S6, Table S5). Of note is that the improved charge carrier mobilities mainly originate from the enhanced crystallinity induced by halogenation, which is supported by the increased crystalline coherence length (CCL) values calculated from the grazing incidence wide angle x-ray scattering (GIWAXS) data (Fig. S7, Table S6). Ultimately, the superior PCE of 9.40% and inferior PCE of 9.11% are obtained in PBDB-T:F-BTA3 and PBDB-T:Cl-BTA3, respectively. In addition, the integrated J_{cal} from the EQE spectra and J_{SC} from the J - V characteristics display errors within 3%.

The indoor photovoltaic performance of these three systems were further measured using a LED (3000 K) lamp as the light source. The integral incident light power density (P_{in}) is calculated to be 296.6 μ W cm⁻² from the emission spectra at 1000 lux (Fig. S8). Under 1000 lux LED light, the PBDB-T:BTA3 cells present the best photovoltaic performance across three systems with a V_{OC} of 0.985 V, a J_{SC} of 100.53 μ A cm⁻², a FF of 75.04%, and a PCE of 25.05% [Fig. 4(c), Table I]. Inferior PCEs of 24.15% and 23.21% are achieved in PBDB-T:F-BTA3 and PBDB-T:Cl-BTA3, respectively. The calculated J_{cal} based on the EQE and photon flux spectra is 99.21 μ A cm⁻² for PBDB-T:BTA3, 105.64 μ A cm⁻² for PBDB-T:F-BTA3, and 106.47 μ A cm⁻²

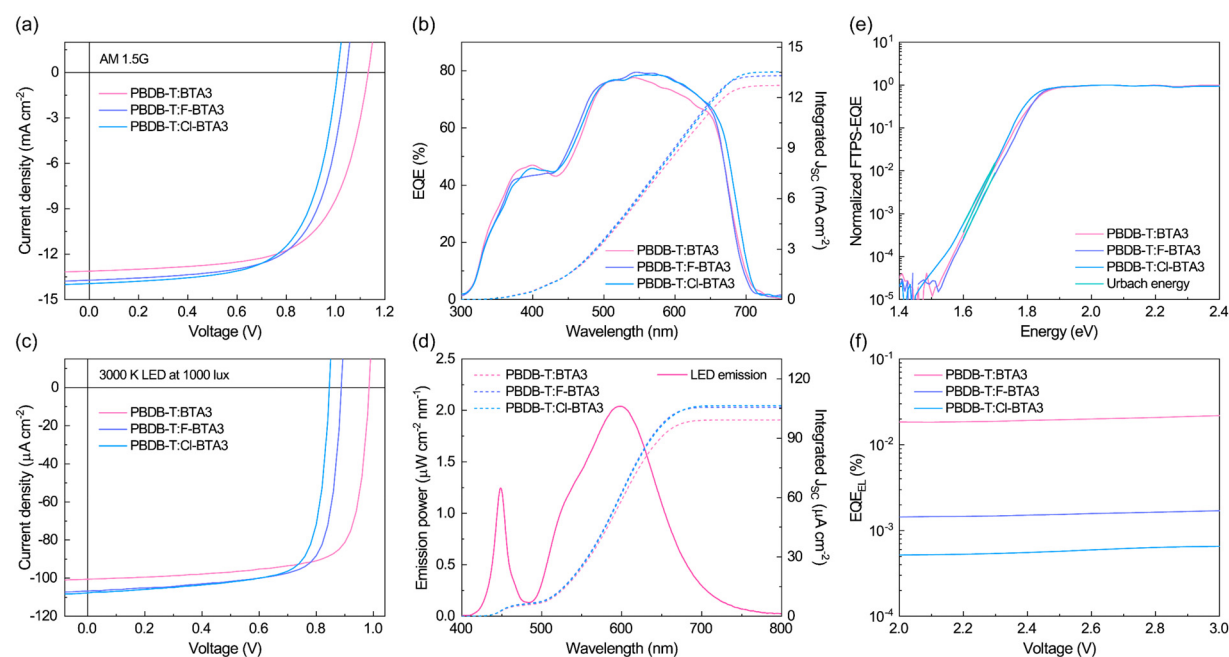


FIG. 4. (a) J - V curves and (b) EQE spectra of the devices measured under one sun illumination. (c) J - V curves and (d) the integral current densities of the devices measured under LED illumination. (e) Normalized FTPS-EQE and (f) EQE_{EL} spectra of the devices.

for PBDB-T:Cl-BTA3 [Fig. 4(d)], thereby confirming the accuracy of J - V measurements.² Although the evolution trends of V_{OC} , J_{SC} , and FF in IOPV cells are consistent with those in outdoor OPV devices, it can be clearly observed that V_{OC} undergoes a more significant attenuation in PBDB-T:F-BTA3 (0.157 V) and PBDB-T:Cl-BTA3 (0.162 V) than PBDB-T:BTA3 (0.147 V) from AM 1.5 G to indoor weak illumination. This finding suggests the increased energy loss in these two devices under indoor illumination. It is reasonably speculated that recombination loss induced by low CT rate may be intensified under low-intensity illumination.

The relevant energy losses (E_{loss}) of the OPV devices were evaluated based on the basics and characterization approaches described in Sec. S1.5 (supplementary material). The non-radiative energy loss (ΔE_{nr}), a major component of E_{loss} , was calculated based on the sensitive EQE spectra measured by Fourier transform photocurrent spectroscopy [FTPS-EQE, Fig. 4(e)] and the EQE spectra of electroluminescence [EQE_{EL}, Fig. 4(f)].^{26,27} The detailed energy loss data are summarized in Table S7. The PBDB-T:BTA3 cells give the smallest ΔE_{nr} and E_{loss} values among these three systems. This

result agrees with the CT rate trend and indicates that low CT rate is more likely to increase non-radiative recombination of CT states. Considering that trap-induced recombination would be enlarged under indoor weak illumination,¹⁵ we measured the density of states (DOS) of trap states by performing capacitance spectroscopy measurements. The details are provided in the supplementary material. As shown in Fig. S9, the density (N_t) and depth (E_t) of trap states are concentrated in $2.33\text{--}2.71 \times 10^{16} \text{ cm}^{-3} \text{ eV}^{-1}$ and 0.117–0.119 eV, which present variation trends opposite to and identical to that of the CT rate, respectively. This phenomenon demonstrates that low CT rate-mediated recombination processes are more affected by deeper energy levels of trap states.²⁸ Thus, in this case, it is more easy to induce additional energy loss for OPV systems with low CT rate from outdoor to indoor illumination owing to significantly decreased density of CT states and intensified impacts of trap states. In addition, the Urbach energy (E_U) parameter was also extracted from the FTPS-EQE spectra. The smallest E_U of 27.35 meV is achieved in PBDB-T:BTA3 cells (Table S7), indicating lowered degree of energetic disorder that reduces radiative

TABLE I. Photovoltaic parameters of PBDB-T:NFA-based OPV devices measured under 3000 K LED light source at 1000 lux intensity.

Device	P_{in} ($\mu\text{W cm}^{-2}$)	V_{OC} (V)	J_{SC} ($\mu\text{A cm}^{-2}$)	J_{cal} ($\mu\text{A cm}^{-2}$)	FF (%)	P_{out} ($\mu\text{W cm}^{-2}$)	PCE ^a (%)
BTA3	296.6	0.985 (0.984 ± 0.002)	100.53 (100.15 ± 0.47)	99.21	75.04 (74.58 ± 0.53)	74.31 (73.50 ± 0.78)	25.05 (24.78 ± 0.26)
F-BTA3	296.6	0.887 (0.885 ± 0.003)	106.75 (106.38 ± 0.44)	105.64	75.65 (75.13 ± 0.59)	71.63 (70.73 ± 0.85)	24.15 (23.85 ± 0.28)
Cl-BTA3	296.6	0.846 (0.844 ± 0.003)	107.79 (107.34 ± 0.52)	106.47	75.48 (74.87 ± 0.66)	68.83 (67.84 ± 0.92)	23.21 (22.87 ± 0.31)

^aThe average parameters were calculated from ten independent cells.

recombination loss below the bandgap.²⁹ Surprisingly, neat and blend films of PBDB-T: BTA3 exhibit the largest Stokes shift between the absorption and PL spectra in three systems (Table S8), suggesting its enlarged excited-state relaxations.²⁰ This optical feature is presumably attributed to the higher degree of energetic disorder for the first excited state (S_1), which theoretically increases the associated energy loss.³⁰ However, our findings underscore that increasing energetic disorder of the excited states does not result in notable recombination of CT states. This is an important point as it indicates reduced limitation on the Stokes shift of photovoltaic materials in designing IOPV cells, deserving more in-depth research and discussion.

In summary, this work reports the CT rate-mediated recombination process in IOPV cells. A global fitting model for quantifying charge generation pathways is proposed, which uncovers an approximately equal ratio ($\sim 50\%$) of conversion from CT states or i-DEs to charge carriers. The overall CT rate including electron and hole transfer is thus obtained under different LUMO and HOMO energetic offsets, and it is free from the i-DEs-dependent exciton dissociation. It is noticed that extremely high driving forces can significantly reduce the CT rate, resulting in the accumulation of CT states at the D:A interfaces that increases the radiative and non-radiative recombination. This low CT rate-induced recombination process is aggravated from outdoor to indoor illumination, which can be the result of reduced exciton density. Thus, the relationship between CT rate and energy loss has been well established in IOPVs. These findings provide photophysical insights to understand the CT rate-mediated energy loss in IOPVs, contributing to improving V_{OC} and thereby to the realization of more efficient IOPV cells.

See the [supplementary material](#) for more details on the fabrication of IOPV cells; experimental and calculation methods; electrostatic potential maps of donor and acceptor materials (Fig. S1); global fitting spectra and dynamics of TAS data (Figs. S2–S4); PL spectra and fluorescence lifetime of neat and blend films (Fig. S5); J - V curves of single carrier devices (Fig. S6). GIWAXS patterns and extracted line cuts (Fig. S7); emission power and integrated power spectra of 3000 K LED at 1000 lux light intensity (Fig. S8); calculated trap density and depth (Fig. S9); energetic offsets of LUMO or HOMO (Table S1); global fitting results of TAS data (Table S2); fitting results of TRPL spectra (Table S3); photovoltaic parameters of solar cells (Table S4); calculated carrier mobility (Table S5); calculated d -spacing and CCL (Table S6); calculated energy loss (Table S7); and extracted Stokes shift parameter (Table S8).

This work was supported by the National Natural Science Foundation of China (Grant Nos. 52203333 and 52320105003) and the Shandong Provincial Natural Science Foundation (ZR2024QA063 and ZR2024QA163). X.T.H. acknowledges receiving support from the Taishan Scholars Program (tstp20230610). K.N.Z. acknowledges receiving support from the Young Scholars Program of Shandong University. We would like to thank the Analytical Centre for Structural Constituent and Physical Property of Core Facilities Sharing Platform, Shandong University, for providing access to the femtosecond transient absorption spectroscopy system (TAS, 2104573S). The authors are grateful to the Shanghai Synchrotron Radiation Facility (beam line BL16B1) for assisting with GIWAXS measurements.

AUTHOR DECLARATIONS

Conflict of Interest

The authors have no conflicts to disclose.

Author Contributions

Kangning Zhang: Data curation (lead); Funding acquisition (equal); Methodology (lead); Validation (lead); Writing – original draft (lead); Writing – review & editing (equal). **Jiawei Qiao:** Data curation (equal); Funding acquisition (equal). **Sixuan Cheng:** Data curation (equal); Validation (equal). **Mingxu Zhou:** Data curation (equal). **Jinqun Xu:** Data curation (equal). **Peng Lu:** Data curation (equal); Writing – review & editing (equal). **Hang Yin:** Writing – review & editing (equal). **Xiaoyan Du:** Writing – review & editing (equal). **Maojie Zhang:** Writing – review & editing (equal). **Xiaotao Hao:** Conceptualization (equal); Funding acquisition (equal); Project administration (lead); Supervision (lead); Writing – review & editing (equal).

DATA AVAILABILITY

The data that support the findings of this study are available from the corresponding author upon reasonable request.

REFERENCES

- Y. Cui, Y. Wang, J. Bergqvist, H. Yao, Y. Xu, B. Gao, C. Yang, S. Zhang, O. Inganäs, F. Gao, and J. Hou, *Nat. Energy* **4**(9), 768 (2019).
- Y. Cui, L. Hong, T. Zhang, H. Meng, H. Yan, F. Gao, and J. Hou, *Joule* **5**(5), 1016 (2021).
- Z. Chen, H. Yin, Z. Wen, S. K. So, and X. Hao, *Sci. Bull.* **66**(16), 1641 (2021).
- Z. Chen, H. Yin, J. K. W. Ho, L. Cui, S. K. So, and X. Hao, *Appl. Phys. Lett.* **118**(4), 043301 (2021).
- Z. Wu, R. Shi, T. Chen, J. Liu, X. Du, Z. Ji, X. Hao, and H. Yin, *Appl. Phys. Lett.* **121**(13), 133905 (2022).
- J. Hou, O. Inganäs, R. H. Friend, and F. Gao, *Nat. Mater.* **17**, 119 (2018).
- C. Li, J. Zhou, J. Song, J. Xu, H. Zhang, X. Zhang, J. Guo, L. Zhu, D. Wei, G. Han, J. Min, Y. Zhang, Z. Xie, Y. Yi, H. Yan, F. Gao, F. Liu, and Y. Sun, *Nat. Energy* **6**(6), 605 (2021).
- J. Wang, Y. Xie, K. Chen, H. Wu, J. M. Hodgkiss, and X. Zhan, *Nat. Rev. Phys.* **6**(6), 365 (2024).
- L. Ma, Y. Chen, P. C. Y. Chow, G. Zhang, J. Huang, C. Ma, J. Zhang, H. Yin, A. M. Hong Cheung, K. S. Wong, S. K. So, and H. Yan, *Joule* **4**(7), 1486 (2020).
- T. Zhang, C. An, Y. Xu, P. Bi, Z. Chen, J. Wang, N. Yang, Y. Yang, B. Xu, H. Yao, X. Hao, S. Zhang, and J. Hou, *Adv. Mater.* **34**(43), 2207009 (2022).
- H. S. Ryu, S. Y. Park, T. H. Lee, J. Y. Kim, and H. Y. Woo, *Nanoscale* **12**(10), 5792 (2020).
- F. Bai, J. Zhang, A. Zeng, H. Zhao, K. Duan, H. Yu, K. Cheng, G. Chai, Y. Chen, J. Liang, W. Ma, and H. Yan, *Joule* **5**(5), 1231 (2021).
- W. Wang, Y. Cui, T. Zhang, P. Bi, J. Wang, S. Yang, J. Wang, S. Zhang, and J. Hou, *Joule* **7**(5), 1067 (2023).
- Q. Wu, Y. Yu, X. Xia, Y. Gao, T. Wang, R. Sun, J. Guo, S. Wang, G. Xie, X. Lu, E. Zhou, and J. Min, *Joule* **6**(9), 2138 (2022).
- Z. Chen, T. Wang, Z. Wen, P. Lu, W. Qin, H. Yin, and X. Hao, *ACS Energy Lett.* **6**(9), 3203 (2021).
- A. J. Gillett, A. Privitera, R. Dilmurat, A. Karki, D. Qian, A. Pershin, G. Londi, W. K. Myers, J. Lee, J. Yuan, S. J. Ko, M. K. Riede, F. Gao, G. C. Bazan, A. Rao, T. Q. Nguyen, D. Beljonne, and R. H. Friend, *Nature* **597**(7878), 666 (2021).
- Y. Wang, J. Yu, R. Zhang, J. Yuan, S. Hultmark, C. E. Johnson, N. P. Gallop, B. Siegmund, D. Qian, H. Zhang, Y. Zou, M. Kemerink, A. A. Bakulin, C. Müller, K. Vandewal, X. Chen, and F. Gao, *Nat. Energy* **8**(9), 978 (2023).
- R. A. Marcus, *Rev. Mod. Phys.* **65**(3), 599 (1993).

- ¹⁹J. Wang, X. Jiang, H. Wu, G. Feng, H. Wu, J. Li, Y. Yi, X. Feng, Z. Ma, W. Li, K. Vandewal, and Z. Tang, *Nat. Commun.* **12**(1), 6679 (2021).
- ²⁰Y. Shi, Y. Chang, K. Lu, Z. Chen, J. Zhang, Y. Yan, D. Qiu, Y. Liu, M. A. Adil, W. Ma, X. Hao, L. Zhu, and Z. Wei, *Nat. Commun.* **13**(1), 3256 (2022).
- ²¹J. Xu, S. B. Jo, X. Chen, G. Zhou, M. Zhang, X. Shi, F. Lin, L. Zhu, T. Hao, K. Gao, Y. Zou, X. Su, W. Feng, A. K. -Y. Jen, Y. Zhang, and F. Liu, *Adv. Mater.* **34**(16), 2108317 (2022).
- ²²K. Jiang, J. Zhang, C. Zhong, F. R. Lin, F. Qi, Q. Li, Z. Peng, W. Kaminsky, S.-H. Jang, J. Yu, X. Deng, H. Hu, D. Shen, F. Gao, H. Ade, M. Xiao, C. Zhang, and A. K. Y. Jen, *Nat. Energy* **7**(11), 1076 (2022).
- ²³T. Dai, Q. Nie, P. Lei, B. Zhang, J. Zhou, A. Tang, H. Wang, Q. Zeng, and E. Zhou, *ACS Appl. Mater. Interfaces* **13**(49), 58994 (2021).
- ²⁴R. Wang, C. Zhang, Q. Li, Z. Zhang, X. Wang, and M. Xiao, *J. Am. Chem. Soc.* **142**(29), 12751 (2020).
- ²⁵K. Zhang, X. Du, J. Qiao, H. Hu, W. Zhang, L. Wang, M. Gao, H. Yin, W. Qin, and X. Hao, *Energy Environ. Sci.* **15**(12), 5261 (2022).
- ²⁶B. Fan, X. Du, F. Liu, W. Zhong, L. Ying, R. Xie, X. Tang, K. An, J. Xin, N. Li, W. Ma, C. J. Brabec, F. Huang, and Y. Cao, *Nat. Energy* **3**(12), 1051 (2018).
- ²⁷L. Zuo, S. B. Jo, Y. Li, Y. Meng, R. J. Stoddard, Y. Liu, F. Lin, X. Shi, F. Liu, H. W. Hillhouse, D. S. Ginger, H. Chen, and A. K. Jen, *Nat. Nanotechnol.* **17**(1), 53 (2022).
- ²⁸J. Zhou, D. He, Y. Li, F. Huang, J. Zhang, C. Zhang, Y. Yuan, Y. Lin, C. Wang, and F. Zhao, *Adv. Mater.* **35**(3), 2207336 (2023).
- ²⁹L. Zhan, S. Li, Y. Li, R. Sun, J. Min, Z. Bi, W. Ma, Z. Chen, G. Zhou, H. Zhu, M. Shi, L. Zuo, and H. Chen, *Joule* **6**(3), 662 (2022).
- ³⁰L. Zhan, S. Yin, Y. Li, S. Li, T. Chen, R. Sun, J. Min, G. Zhou, H. Zhu, Y. Chen, J. Fang, C. Q. Ma, X. Xia, X. Lu, H. Qiu, W. Fu, and H. Chen, *Adv. Mater.* **34**(45), 2206269 (2022).